

1 **Impact of convectively lofted ice on the seasonal cycle of water vapor** 2 **in the tropical tropopause layer**

3 Xun Wang¹, Andrew E. Dessler¹, Mark R. Schoeberl², Wandu Yu¹, and Tao Wang³

4 ¹Department of Atmospheric Sciences, Texas A&M University, College Station, TX, USA

5 ²Science and Technology Corporation, Columbia, MD, USA

6 ³University of Maryland, College Park, MD, USA

7 *Correspondence to:* Andrew E. Dessler (adessler@tamu.edu)

8 **Abstract.** We use a forward Lagrangian trajectory model to diagnose mechanisms that produce water vapor seasonal cycle
9 observed by the Microwave Limb Sounder (MLS) and reproduced by the Goddard Earth Observing System Chemistry
10 Climate Model (GEOSCCM) in the tropical tropopause layer (TTL). We confirm in both the MLS and GEOSCCM that the
11 seasonal cycle of water vapor entering the stratosphere is primarily determined by the seasonal cycle of TTL temperatures.
12 However, we find that the seasonal cycle of temperature predicts a smaller seasonal cycle of TTL water vapor between
13 10°N-40°N than observed by MLS or simulated by the GEOSCCM. Our analysis of the GEOSCCM shows that including
14 evaporation of convective ice in the trajectory model increases both the simulated maximum value of the 100-hPa 10°N-
15 40°N water vapor seasonal cycle as well as increasing the seasonal-cycle amplitude. We conclude that the moistening effect
16 from convective ice evaporation in the TTL plays a key role regulating and maintaining seasonal cycle of water vapor in the
17 TTL. Most of the convective moistening in the 10°N-40°N range comes from convective ice evaporation occurring at the
18 same latitudes. A small contribution to the moistening comes from convective ice evaporation occurring between 10°S-
19 10°N. Within the 10°N-40°N band, the Asian monsoon region is the most important region for convective moistening by ice
20 evaporation during boreal summer and autumn.

21 **1 Introduction**

22 Stratospheric water vapor is important for the radiative budget of the atmosphere and the regulation of stratospheric ozone
23 (e.g., Solomon et al., 1986; Dvortsov and Solomon, 2001). One of the key features of the tropical lower stratospheric (LS)
24 water vapor is its seasonal cycle often referred to as the "tape recorder" (Mote et al., 1995, 1996). The amount of water vapor
25 entering the stratosphere and its seasonal cycle is primarily controlled by temperatures in the tropical tropopause layer (TTL)
26 (Brewer, 1949; Holton et al., 1995; Fueglistaler et al., 2009). The low TTL temperatures freeze-dry the air, reducing the
27 water vapor mixing ratios and imprinting the seasonal cycle on air ascending into the stratosphere through the TTL (e.g.,
28 Mote et al., 1996; Fueglistaler, 2005; Schoeberl et al., 2008; Fueglistaler et al., 2009).

29 Analyses of observations have suggested that deep convection reaching the TTL may also be important for regulating the

30 amount of water vapor entering the stratosphere. Nielsen et al. (2007) and Corti et al. (2008) suggested that deep penetrating
31 convection deposits ice particles above the cold point tropopause, where ice may evaporate and cause a moistening effect.
32 This idea is also supported by observations of enrichment of the deuterated isotopologue of water vapor (HDO) in the
33 tropical LS (Moyer et al., 1996; Dessler et al., 2007; Steinwagner et al., 2010). The role of convective ice evaporation in the
34 stratospheric entry water vapor has also been addressed in several model studies. Schoeberl et al. (2014, 2018, 2019)
35 quantified the global impact of convective ice on winter 2008/2009 water vapor between 18-30 km, and concluded that, for
36 global average water vapor between 18-30 km during winter, the convective ice evaporation plays a small role, since
37 convection rarely reach the level of the tropopause cold point. During El Niño events, convective ice evaporation appears to
38 play a larger role in the interannual variability of TTL and LS water vapor (Avery et al., 2017; Ye et al., 2018). On longer
39 time scales, convective ice evaporation was found to contribute to an important fraction of the increase of stratospheric entry
40 water vapor over the next century in two chemistry-climate models (Dessler et al., 2016).

41 The goal of this paper is to investigate the impact of convective moistening on the seasonal cycle of water vapor entering the
42 stratosphere. Previous analyses have separately investigated the winter/summer impact, interannual variability, and the long-
43 term trend (Ueyama et al., 2015, 2018; Dessler et al., 2016; Avery et al., 2017; Schoeberl et al., 2014, 2018; Ye et al., 2018).
44 However, less work has been done on understanding the impact of convective ice on the seasonal cycle. The basics of the
45 water vapor seasonal cycle can be understood simply: more water vapor enters the LS during boreal summer, when TTL
46 temperatures are generally higher and vice versa during boreal winter. Observations (Fig. 1a-c) reveal that zonal mean water
47 vapor is observed to have a larger amplitude seasonal cycle in the NH subtropics near the tropopause level (e.g., Rosenlof,
48 1997; Randel et al., 1998, 2001, and references therein), despite the fact that the temperature seasonal cycle is symmetric
49 about the equator (Figs. 1b-c). We will refer to this as “the hemispheric asymmetry”. At higher altitudes, the hemispheric
50 asymmetry gradually disappears (Fig. 1a) (e.g., Randel et al., 1998, 2001).

51 Previous studies have suggested that this hemispheric asymmetry structure in the water vapor seasonal cycle is due to
52 processes within the Southeast Asian monsoon and North American monsoon region, including both diabatic and adiabatic
53 transport in the TTL (Rosenlof, 1997; Randel et al., 1998; Dethof et al., 1999; Bannister et al., 2004; Gettelman et al., 2004;
54 Pan et al., 1997, 2000, Park et al., 2004, 2007; Wright et al., 2011; Ploeger et al., 2013). Indeed, the MLS data (Fig. 2c) show
55 that the summertime maxima of the 100-hPa water vapor is confined in the Asian monsoon and North American monsoon
56 anti-cyclones (Rosenlof, 1997; Jackson et al., 1998; Randel et al., 1998, 2001; Dessler and Sherwood, 2004; Randel and
57 Park, 2006; Park et al., 2007; Bian et al., 2012) and become weaker above 100 hPa (Figs. 2a-b).

58 Many previous studies have investigated impact of convection within the monsoon regions on the budget of the stratospheric
59 entry water vapor. Dessler and Sherwood (2004) used a budget model with and without convection and concluded that,
60 during summer, moistening by deep penetrating convection increases the northern hemisphere (NH) extratropical water
61 vapor at 380-K isentrope by 40%. Fu et al. (2006) suggested that the deep convection over the Tibetan Plateau acts as a short

62 circuit of water vapor ascending across the tropical tropopause. James et al. (2008) used a trajectory model and concluded
63 that air parcels are lifted by convection over Southeast Asia and then transported into the TTL by the monsoon anticyclone,
64 avoiding the cold pool in the deep tropics. However, they pointed out that direct convective injection has a limited impact on
65 the 100-hPa water vapor budget, contributing to 0.3 ppmv of the water vapor in the Asian monsoon region. Schwartz et al.
66 (2013) provided evidence of occasional enhanced 100-hPa and 82.5-hPa water vapor by convective injection over the Asian
67 and North American monsoon regions using satellite observations. Randel et al. (2015) investigated subseasonal variations
68 in 100-hPa water vapor in NH monsoon regions and suggested that stronger convection leads to lower TTL temperatures in
69 the monsoon regions, which results in less LS water vapor there, thereby concluding that the LS water vapor in the monsoon
70 regions is mainly controlled by large-scale transport and TTL temperatures there. Ueyama et al. (2018) investigated the
71 convective moistening effect on 100-hPa water vapor during boreal summer. They used a trajectory model that includes
72 cloud formation, gravity waves, and convective moistening and concluded that convection moistens the water vapor
73 averaged over 10°S-50°N by 0.6 ppmv (~15%) and that convective moistening over the Asian monsoon region plays an
74 important role.

75 The role of convective ice evaporation in the TTL during boreal summer is still under debate. Furthermore, its impact on the
76 TTL water vapor seasonal cycle has not been fully explored. In this study, we quantitatively investigate the impact of
77 convective ice evaporation on the seasonal cycle of water vapor in the TTL.

78 **2 Models and Data**

79 **2.1 MLS water vapor**

80 We analyze here version 4.2 level 2 water vapor retrieved from the Earth Observing System (EOS) Microwave Limb
81 Sounder (MLS) instrument on the Aura spacecraft (Livesey et al., 2017). Since August 2004, the MLS provides ~3500
82 vertical scans of the earth's limb from the surface to 90 km each day, covering a latitude range of 82°S to 82°N with a
83 horizontal resolution of 1.5° along the orbit track (Lambert et al., 2007). The MLS water vapor retrieval has a vertical
84 resolution of about 3 km in the TTL, with precision at 100 hPa and 82.5 hPa of 15% and 7%, respectively. The accuracy of
85 the water vapor at 100 hPa and 82.5 hPa is 8% and 9%, respectively (Livesey et al., 2017). We composite the daily standard
86 water vapor between August 2004 to October 2018 to produce monthly means on a horizontal grid of 4° latitude by 8°
87 longitude following the data-screening in Livesey et al., (2017).

88 **2.2 Ice Water Content from Cloud-Aerosol Lidar with Orthogonal Polarization**

89 The Cloud-Aerosol Lidar with Orthogonal Polarization (CALIOP) is a two-wavelength polarization elastic backscatter lidar
90 that detects global tropospheric and lower stratospheric aerosol and cloud profiles (Hu et al., 2009; Liu et al., 2009; Vaughan
91 et al., 2009; Winker et al., 2009, 2010; Young and Vaughan, 2009; Avery et al., 2012; Heymsfield et al., 2014). We use the

92 CALIOP Level 2 Cloud Profile Product in version 4.2, with horizontal resolution of 5 km along-track and 60 m vertically in
93 the TTL and LS. The CALIOP cloud Ice Water Content (IWC) is derived from a parameterized function of the CALIOP 532
94 nm cloud particle extinction profiles (Avery et al., 2012; Heymsfield et al., 2014). We use the IWC from all clouds minus the
95 IWC from thin cirrus clouds (clouds that are not opaque) above 146 hPa, which is a rough estimate of convective ice in the
96 TTL region, since the CALIOP does not separate convective from non-convective IWC measurements. These CALIOP IWC
97 data, obtained between May 2008 and December 2013, are then monthly averaged onto the same horizontal and vertical
98 grids as were used for the MLS data.

99 **2.3 GEOSCCM**

100 We also analyze simulations from the Goddard Earth Observing System Chemistry Climate Model (GEOSCCM). The
101 GEOSCCM couples the GEOS-5 general circulation model (Rienecker et al., 2008; Molod et al., 2012) to a comprehensive
102 stratospheric chemistry module (Oman and Douglass, 2014; Pawson et al., 2008). The GEOSCCM uses a single-moment
103 cloud microphysics scheme (Bacmeister et al., 2006; Barahona et al., 2014). The run analyzed here starts in 1998 and ends in
104 2099 and driven by the Representative Concentration Pathway (RCP) 6.0 greenhouse gas scenario (Van Vuuren et al., 2011)
105 and the A1 scenario for ozone depleting substances (World Meteorological Organization, 2011). Sea surface temperatures
106 and sea ice concentrations were prescribed from Community Earth System Model version 1 simulations (Gent et al., 2011).
107 The model has a horizontal resolution of 2°latitude by 2.5°longitude and 72 vertical levels up to the model top at 0.01 hPa
108 (Molod et al., 2012).

109 **2.4 Trajectory Model**

110 We also use the forward, domain filling, diabatic trajectory model described in Schoeberl and Dessler (2011) and updated in
111 subsequent publications. The trajectory model uses 6-hourly instantaneous horizontal winds and 6-hourly average diabatic
112 heating rates to advect parcels using the Bowman trajectory code (Bowman, 1993; Bowman and Carrie, 2002).
113 Meteorological fields used to drive the model in this paper come from the European Centre for Medium-Range Weather
114 Forecasts (ECMWF) ERA-interim (ERAi), and Modern-Era Retrospective analysis for Research and Applications-2
115 (MERRA-2) (Molod et al., 2015; Gelaro et al., 2017), and the GEOSCCM.

116 In this study, the trajectory model initializes 1350 parcels daily in the upper troposphere on an equal area longitude-latitude
117 grid covering 0-360°longitude and $\pm 60^\circ$ latitude, and with initial water vapor mixing ratio of 200 parts per million by volume
118 (ppmv). This value is well above saturation, so the parcels are dehydrated to saturation after the first time step of the
119 trajectory model run. Sensitivity tests show that our results are not impacted by the initialization values.

120 The initialization level is at 360-K potential temperature, which is above the average level of zero heating (~ 355 -360 K)
121 (Fueglistaler et al., 2009) but below the tropical cold point. In the MERRA-2, the average heating rates below ~ 365 K in the

122 NH subtropics are negative during boreal summer (not shown), which results in parcels in that region immediately
123 descending back to the troposphere after initialization. To deal with this problem, we initialize parcels at 360 K in MERRA-
124 2 simulations. But if the local heating rate at 360 K is negative, we raise the initialization level to the lowest isentropic level
125 with positive heating rate at the same horizontal position. However, we note that the level of zero heating rate is higher
126 (~370 K) over the NH monsoon regions in MERRA-2. Releasing parcels at ~370 K over the NH monsoon regions results in
127 insufficient dehydration and a moist bias there (Schoeberl et al., 2013; Ueyama et al., 2018). To avoid this bias, we set the
128 local initialization level to 366 K (1 K above the tropical average level of zero heating rate) for those parcels. At the end of
129 each day, parcels below the 250-hPa pressure surface or above the 5000-K isentrope are removed because they are
130 considered outside of the model boundaries. We note that the parcels initialized at mid-latitudes mostly descend into the
131 troposphere.

132 Along each trajectory, an instant dehydration scheme is used. In this scheme, anytime the relative humidity (hereafter RH,
133 always with respect to ice) exceeds the dehydration threshold, water vapor is instantly removed to reduce the parcel's RH to
134 the dehydration threshold. The RH calculation uses 6-hourly temperatures linearly interpolated in time and space to parcel
135 locations at each time step; the RH is computed using the saturation mixing ratio at that temperature Murphy and Koop
136 (2005). The pre-set dehydration threshold is 100% RH for the ERAi trajectory runs and MERRA-2 trajectory runs. For the
137 GEOSCCM trajectory runs, the pre-set dehydration threshold is 80% RH, since in the GEOSCCM dehydration occurs when
138 the grid-average RH is around this value (Molod et al., 2012). The same parameterization for the pre-set RH threshold of
139 80% was used successfully analyzing the water vapor interannual variability in the GEOSCCM in Dessler et al. (2016) and
140 Ye et al. (2018). We will refer to this version as the “standard” trajectory model – another version that includes ice
141 evaporation will be introduced later.

142 As an alternative to instant dehydration we can run a cloud model along the trajectory model, which is described in
143 Schoeberl et al. (2014). The cloud model triggers ice nucleation at a prescribed nucleation RH (NRH) threshold and the
144 number of ice particles produced upon nucleation is proportional to the parcel cooling rate using the relationship derived by
145 Kärcher et al. (2006). The ice mixing ratio is carried with the parcel along with number of crystals and size. Ice crystal
146 distribution has a single size mode that varies as the parcels grow or sublimate. Gravitational sedimentation reduces the total
147 ice amount within the parcel. Ice crystals are assumed to be spheres which is reasonable for small crystals in the upper
148 troposphere (Woods et al., 2018). The cloud model uses a fixed cloud geometrical thickness of 500 m based on the TTL
149 cloud thickness distribution observed by CALIOP (Schoeberl et al., 2014). We also assume that ice falling out of the cloud
150 slowly sublimates in sub-saturated layers well below the cloud. The cloud model incorporates more realistic physics than the
151 instant dehydration scheme we use in the standard trajectory model and it produces good agreement with observational data
152 from aircraft flights (Schoeberl et al., 2015). The physics in the cloud model has a net effect of slowing down the parcels'
153 dehydration rate and increasing water vapor in the LS compared to the instant dehydration scheme (Schoeberl et al., 2014).

154 All the trajectory model runs include methane oxidation as a water source as described in Schoeberl and Dessler (2011), but
155 this process is unimportant in the TTL and LS. We start all trajectory models on 1/1/2000 and analyze the model results from
156 2005 to October 2018, so that we can compare the ERAi and MERRA-2 driven trajectory results to the MLS observations.
157 The GEOSCCM is a free-running model, so interannual variability of the model will not match MLS observations. We will
158 therefore compare a multi-year average of the GEOSCCM to observations.

159 **3 Results**

160 **3.1 Impact of convective moistening on the seasonal cycle**

161 Figures 1d-i show the water vapor seasonal cycle at 100 hPa, 82.5 hPa, and 68 hPa simulated by the standard trajectory
162 model driven by ERAi, and MERRA-2 in which dehydration is entirely driven by temperature and there is no convective
163 influence (See Table 1 for summary of the trajectory model cases). To compare with the MLS, we averaged the trajectory
164 water vapor fields in the vertical using the MLS averaging kernels following the instructions from Livesey et al. (2017). The
165 trajectory models fail to produce the hemispheric asymmetry, the larger water vapor seasonal cycle in the NH subtropics in
166 August-September at 100 hPa and 82.5 hPa (Figs. 1e-f and 1h-i). Specifically, the ERAi and MERRA-2 trajectory models
167 underestimate the 100-hPa seasonal amplitude over 10°N-40°N by 0.5 ppmv (24%) and 0.89 ppmv (43%) respectively. At
168 68 hPa, the trajectory models agree with the MLS that the seasonal cycle is approximately centered over the equator,
169 although they underpredict the MLS (Figs. 1a, 1d, and 1g). During June-July-August (JJA) (Figs. 2d-i), the trajectory models
170 underestimate the maxima over the Asian and North American monsoon regions (Figs. 2e-f, 2h-i), which agrees with
171 Ueyama et al. (2018) who also showed that the trajectory model driven by the ERAi without any convective influence fails
172 to reproduce the boreal summer maxima. At 68 hPa, the monsoonal maxima are nearly gone (Figs. 2d and 2g).

173 We also ran the ERAi and MERRA-2 simulation with the cloud model described in Section 2.4 operating along the
174 trajectory model, with 100% NRH (Table 1). Note that this version of the trajectory model does not have any convective ice
175 in it, so water vapor is still regulated entirely by TTL temperatures. Figures 1j-o show that the cloud model produces larger
176 water vapor values in the seasonal cycles at 100 hPa, 82.5 hPa, and 68 hPa. There is also a slight increase in the seasonal
177 maximum poleward of 20°N (Figs 1l and 1o) at 100 hPa. The ERAi and MERRA-2 trajectory models with the cloud model
178 increase the 10°N-40°N seasonal amplitude at 100 hPa by 0.1 ppmv (6%) and 0.08 ppmv (7%) - a small improvement
179 compared to the instant dehydration scheme. However, the cloud model doesn't help reproduce the observed hemispheric
180 asymmetry in the seasonal cycles at 100 hPa and 82.5 hPa – it basically increases water vapor both north and south of the
181 equator. During JJA (Figs. 2l and 2o), the cloud model increases the 100-hPa water vapor values over the Asian monsoon
182 and North American monsoon regions, but there is still an underestimation compared to the MLS. We note that the NRH
183 threshold of 100% can be too low, since previous observations showed that the NRH can be as high as 160%-170% in the

184 TTL region during winter (Jensen et al., 2013). Schoeberl et al. (2016) showed that the sensitivity of trajectory simulated
185 water vapor to the NRH threshold is 0.1-0.2 ppmv per 10 percent NRH, and that an NRH threshold of 140-145% in the
186 trajectory model produces water vapor in better agreement with the MLS observations during winter. However, our result
187 regarding the hemispheric asymmetry and boreal summer maxima agrees with Ueyama et al. (2018), who set the NRH
188 threshold to 160%, indicating that the hemispheric asymmetry is not sensitive to the choice of NRH threshold. Thus,
189 regardless of dehydration scheme, models that regulate water vapor only through TTL temperatures and large-scale transport
190 do not reproduce important features of the 100 – 82.5 hPa water vapor seasonal cycle, including the observed hemispheric
191 asymmetry.

192 Our hypothesis is that convective moistening is causing the hemispheric asymmetry in the TTL water vapor seasonal cycle.
193 Previous analyses (e.g., Ueyama et al., 2018) have attempted to test this idea by directly incorporating observed convection
194 into the trajectory model and then evaluating how agreement with water vapor observations improved. However, estimating
195 convective height from passive infrared measurements is difficult and Ueyama et al. (2018) noted that errors in the
196 convective heights created issues in their analysis. Given this significant uncertainty in an observation-only approach, we
197 therefore take a different tack. We perform a parallel analysis with the GEOSCCM, a model that we show below reproduces
198 the hemispheric asymmetry and we will examine the causes of the asymmetry in that model and then evaluate whether we
199 think that is what is going on the real world.

200 In our analysis, we first run the standard trajectory model driven by meteorology from the GEOSCCM which, like the
201 standard models analyzed above, uses instant dehydration to regulate water vapor exclusively through TTL temperatures.
202 We also run a second version of the trajectory model, the “ice model”, in which we add the convective moistening to the
203 trajectory model.

204 The GEOSCCM outputs convective ice at every step. To add convective moistening to our trajectory model, we linearly
205 interpolate the GEOSCCMs’ 6-hourly three-dimensional convective ice field to the location and time of each trajectory’s
206 time step. Then, at each time step, we assume complete evaporation of the ice into the sub-saturated parcels by adding the ice
207 water content to the parcels’ water vapor — although we do not let parcels exceed the pre-set RH threshold of 80%. This is
208 similar to the convective moistening scheme used by Schoeberl et al. (2014), who used MERRA anvil ice to facilitate the
209 convective moistening in the trajectory model. After each encounter, we do not allow parcels to carry any remaining
210 convective ice downstream as Schoeberl et al. (2014) did in their ASC case. Ueyama et al. (2018) used a similar convective
211 moistening scheme, where they saturated the column model up to the observed cloud top when a parcel’s trajectory
212 intersects a convective cloud. Because we assume instant dehydration and instant evaporation of the ice, we consider the
213 convective moistening in our trajectory model runs to be an upper limit of the impact of convective ice evaporation on the
214 TTL water content in the GEOSCCM (Dessler et al., 2016).

215 To test if GEOSCCM convective ice field is realistic, we compare GEOSCCM convective ice with CALIOP ice data (ppmv)
216 (Figures 3 and 4). For the CALIOP, we show IWC from all clouds minus IWC from thin cirrus clouds (not opaque), above
217 146 hPa, which is a rough estimate of convective ice in the TTL region, although it is almost certainly an underestimate of
218 true convective ice amount. There's general agreement between the spatial pattern of GEOSCCM and CALIOP convective
219 ice. However, the GEOSCCM generally produces more convective ice and higher convective top altitudes than the CALIOP.
220 To address these problems in the GEOSCCM, we also show the GEOSCCM convective ice field reduced by 80% (0.2ice),
221 which brings tropical GEOSCCM convective ice into better agreement with the CALIOP values at 121 hPa and above (Figs.
222 3e-f and 4e-f). We show below two sensitivity tests that show our results are not sensitive to the overestimation of
223 convective IWC and convective top altitude by the GEOSCCM.

224 The water vapor seasonal cycles from the GEOSCCM and various GEOSCCM trajectory model runs (Table 1) are shown in
225 Fig. 5. These have been re-averaged in the vertical using the MLS averaging kernels (Livesey et al., 2017) to facilitate
226 comparison with MLS. We focus on the 100-hPa level, where the hemispheric asymmetry is strongest. We note that the 100-
227 hPa level is in the TTL and is not strictly above the tropopause, especially in the summer NH monsoon region. However,
228 processes on this level play a key role in determining stratospheric water vapor (Fueglistaler et al., 2009).

229 The GEOSCCM reproduces the hemispheric asymmetry seen in the MLS observations (compare Fig. 5a with Fig. 1c), and
230 shows that during JJA the 100-hPa water vapor maxima are located over the Asian monsoon and North American monsoon
231 regions (compare Fig. 5b with Fig. 2c). The standard trajectory model driven by GEOSCCM meteorology, which regulates
232 water entirely through TTL temperatures, does not reproduce the hemispheric asymmetry (Fig. 5c). That model also
233 underestimates the JJA water vapor values in the Asian monsoon region and North American monsoon region (Fig. 5d).
234 These results are similar to the comparison between MLS and the standard trajectory models driven by ERAi and MERRA-2
235 (Figs. 1f, 1i, 2f, and 2i)

236 Fig. 6 shows the 100-hPa water vapor seasonal cycles in the NH subtropics (10°N-40°N), deep tropics (10°S-10°N), and
237 southern hemispheric subtropics (10°S-40°S). To aid in comparison, we have subtracted the annual mean from each data set.
238 The standard model generally agrees well with the GEOSCCM and MLS in the 10°S-10°N and 10°S-40°S region (Figs. 6b-
239 d). This suggests that the water vapor seasonal cycle in those regions is mainly controlled by the TTL temperatures and
240 large-scale transport and implying that other factors, including convective ice evaporation, are less important. In the 10°N-
241 40°N region, however, the standard model does a poor job, underestimating the MLS and GEOSCCM seasonal amplitude by
242 1.15 ppmv (55%) and 1.23 ppmv (57%) (Figs. 6a and 6d).

243 If we add convective ice evaporation to the trajectory model, then the models show a clear hemispheric asymmetry in the
244 100-hPa water vapor seasonal cycle and more pronounced seasonal maxima over the monsoon regions (Figs. 5e-h). Fig. 6
245 shows that the ice model and the 0.2ice model (the trajectory model where we add 0.2ice as shown in Figs. 3e-f) produce

246 boreal summer and autumn water vapor values in the 10°N–40°N much closer to the GEOSCCM and MLS. The ice model
247 and the 0.2ice model increase the 10°N–40°N seasonal maximum by 2.39 ppmv (63%) and 1.65 ppmv (44%), and increase
248 the seasonal amplitude by 1.55 ppmv (169%) and 1.03 ppmv (112%) (Figs. 6a and 6d). This means convective ice
249 evaporation is particularly important to the 100-hPa water vapor mixing ratio in NH subtropics during boreal summer and
250 autumn, thereby playing a key role in the seasonal cycle there.

251 Fig. 5e shows that our ice model generates too much water vapor, consistent with too much IWC in the TTL. Given that the
252 GEOSCCM’s water vapor fields are reasonable (e.g., Fig. 5a vs. Fig. 1c), this further emphasizes that our instant dehydration
253 model evaporates too much water vapor, thus yielding an upper limit of the impact of ice evaporation. It may also indicate a
254 cancelling error in the GEOSCCM: too much water from ice cancelling a too low dehydration threshold (80%). Clearly,
255 more research on this question is warranted.

256 We ran another GEOSCCM trajectory ice model to test the sensitivity of water vapor at 100 hPa to convective ice altitude.
257 This was in response to our observation that convective ice in the GEOSCCM went too high into the stratosphere compared
258 to the CALIOP (Fig. 3a vs. Fig. 3c), and we wanted to see if this influences our results. In this test run, we do not allow any
259 ice above the 90-hPa surface to evaporate, so that we eliminate any convective influence that is above that altitude. The
260 zonal mean seasonal cycle and JJA water vapor at 100 hPa from this run is shown in Figs. 5i–j. The difference between the
261 seasonal cycles from the ice model and this test run is less than 0.3 ppmv between 30°S – 30°N. The larger moisture
262 difference at higher latitudes comes from convective moistening in the lowermost stratosphere. However, the hemispheric
263 asymmetry is well reproduced by this test run. We thereby conclude that the impact of convective ice evaporation on the
264 100-hPa water vapor seasonal cycle is insensitive to convective ice occurrence that is too high in altitude.

265 These results suggest that convective ice evaporation in the TTL is important to the 100-hPa water vapor seasonal cycle in
266 the NH subtropics in the GEOSCCM. Combined with the fact that the GEOSCCM has reasonable water vapor and
267 convective fields, and that our results are insensitive to errors in the IWC amount and convective altitudes in the
268 GEOSCCM, we believe this is a plausible explanation for the hemispheric asymmetry. That plausibility is strongly supported
269 by the lack of a competing hypothesis for the asymmetry.

270 **3.2 Source regions of convective ice evaporation**

271 Our result begs the question of which region contributes most to this convective moistening? Here we define the quantity *net*
272 *convective moistening* to be the water vapor mixing ratio in the ice model minus that in the standard trajectory model. The
273 net convective moistening thus represents the net water vapor added by convective ice evaporation. In this section, we
274 investigate the regional contribution to net convective moistening in the NH subtropics in the GEOSCCM, so we don’t use
275 the MLS averaging kernels in the vertical direction, as we did in Section 3.1. The net convective moistening in the NH

276 subtropics seasonal maximum and seasonal amplitude is therefore 2.69 ppmv and 1.68 ppmv – slightly different from the
277 values we show in Fig. 5. We also note that the 100-hPa net convective moistening value in the 10°S - 50°N domain
278 produced by our GEOSCCM analysis during boreal summer is larger than the value of 0.6 ppmv produced by the
279 observational analysis of Ueyama et al. (2018)’s observational analysis. This is because the combination of instant
280 dehydration scheme and instant ice evaporation scheme we use in the trajectory model lead to larger net convective
281 moistening. This also reinforces the idea that the ice model we use in this paper provides an upper limit of the impact of
282 convective ice evaporation on the 100-hPa water content in the GEOSCCM (Dessler et al., 2016). Thus, we view our results
283 to mainly be qualitatively useful.

284 We also quantify the *convective evaporation rate* in the ice model. To do this, we record the location and amount of water
285 vapor added to each parcel from ice evaporation on every time step. We then grid and average these values to produce a
286 three-dimensional field of the ice evaporation rate (in units of ppmv day⁻¹). Note that water vapor added by convection will
287 not necessarily make it into the stratosphere — the added water vapor may be removed in subsequent dehydration events.

288 Fig. 7a and 7b show that convective evaporation rate generally follows the IWC. However, we see that the highest ice
289 evaporation rates and net convective moistening (Fig. 7d) in regions where IWC is high and RH (Fig. 7c) is low (Dessler and
290 Sherwood, 2004). In regions where both IWC and RH are high, evaporation is suppressed, and any air that is moistened by
291 evaporation is rapidly re-dehydrated.

292 To determine how evaporation in different regions contribute to the 10°N-40°N seasonal cycle, we separately track the
293 amount of water vapor produced by evaporation in specific latitude bands. Fig. 8 shows the seasonal cycle of net convective
294 moistening at 100 hPa averaged in the 10°N-40°N region contributed by evaporation of convective ice between 10°N-40°N
295 and 10°S-10°N. We note that, to obtain the net convective moistening and fractions contributed by specific latitude bands,
296 we have not subtracted annual mean from the seasonal cycles in this plot like we did in Fig. 6.

297 During the winter (DJF), contributions from ice evaporation between 10°S-10°N and 10°N-40°N are about even, with
298 slightly larger contribution from 10°S-10°N. During the summertime (JJA), however, evaporation of convective ice in the
299 10°N-40°N region is the dominant contributor to the net convective moistening. Specifically, it contributes to 63% (1.7
300 ppmv) and 59% (0.9 ppmv) of the net convective moistening in the 10°N-40°N water vapor seasonal maximum (September)
301 value and seasonal amplitude, respectively. Convective ice evaporation between 10°S-10°N plays a smaller role,
302 contributing to 31% (0.83 ppmv) and 17% (0.28 ppmv).

303 Next, we investigate net convective moistening in the 100-hPa 10°N-40°N water vapor seasonal cycle contributed by
304 specific regions within the 10°S-40°N domain. To do this, we divide the 10°S-40°N domain into 12 equal-area boxes. We
305 average the net convective moistening contributed by each of these boxes using the same method we used to calculate the

306 contribution by 10°N-40°N and 10°S-10°N. Fig. 9 shows the contribution from each box region to the net convective
307 moistening in the 100-hPa 10°N-40°N water vapor seasonal maximum value in September and the seasonal amplitude.

308 We find that contribution from the box regions over Southeast Asia (10°N-40°N, 60°E-120°E), subtropical Western Pacific
309 (10°N-40°N, 120°E-180°E), and North America (10°N-40°N, 120°W-60°W) dominate. The Southeast Asia region is most
310 important, contributing to 20% (0.54 ppmv) and 20% (0.3 ppmv) of the net convective moistening in the 10°N-40°N water
311 vapor seasonal maximum value and seasonal amplitude, respectively. This conclusion is consistent with Ueyama et al.
312 (2018), who showed that parcels in the 10°S-50°N domain at 100 hPa are mainly hydrated by convection over Southeast
313 Asia. Specifically, they showed that convection over the Asian monsoon region (0-40°N, 40°E-140°E) contributes
314 approximately 50% of the total convective moistening (10°S-50°N) at 100 hPa during August 2007. We computed the
315 contribution from the same domain and got a contribution of 36%. The reason we produce a smaller contribution from this
316 domain is that the GEOSCCM produces more convective ice over the tropical west Indian Ocean (Fig. 4), which results in
317 larger convective moistening contributed by that region.

318 The subtropical Western Pacific also contributes to the net convective moistening in the 100-hPa 10°N-40°N water vapor
319 seasonal cycle. This is due to the abundant convective ice over the subtropical west Pacific (Fig. 4b), which is likely related
320 to the east-west oscillation of the Asian monsoon anticyclone (Pan et al., 2016; Luo et al., 2018). The North America region
321 is less important in the ice model, contributing to 12% (0.3 ppmv) and 13% (0.21 ppmv) of the net convective moistening in
322 the 10°N-40°N water vapor seasonal maximum value and seasonal amplitude. The GEOSCCM underestimates the observed
323 convective ice over the North American monsoon above 120 hPa (not shown), which may cause the contribution from the
324 North American region to be underpredicted.

325 **4 Summary**

326 In this study, we investigated mechanisms that drive the seasonal cycle of water vapor in the TTL. We use a Lagrangian
327 trajectory model (Schoeberl and Dessler, 2011) to analyze the seasonal cycle in observations of water vapor made by the
328 Microwave Limb Sounder (MLS) (Lambert et al., 2007; Livesey et al., 2017) as well as simulated fields from the Goddard
329 Earth Observing System Chemistry Climate Model (GEOSCCM) (Rienecker et al., 2008; Molod et al., 2012; Pawson et al.,
330 2008; Oman and Douglass, 2014).

331 Water vapor's seasonal cycle in the TTL and tropical lower stratosphere (LS), sometimes referred to as the "tape recorder,"
332 has highest values of water vapor entering the stratosphere during NH summer. We confirm in both the MLS observations
333 and in the GEOSCCM that this is mainly due to the seasonal cycle of TTL temperatures. However, closer examination of the
334 data reveals some deficiencies in this simple picture. Both the MLS and GEOSCCM show that the water vapor seasonal
335 cycle in the TTL has a hemispheric asymmetry, with maximum seasonal cycle between 10°N-40°N, despite the fact that the

336 TTL temperature seasonal cycle is symmetric about the equator (e.g., Rosenlof, 1997; Randel et al., 1998, 2001, and
337 references therein). The hemispheric asymmetry is strongest at 100 hPa. Trajectory models that only regulate TTL and
338 tropical LS water vapor using temperatures (Schoeberl and Dessler, 2011) from ERAi, MERRA-2, and GEOSCCM all
339 produce weaker water vapor seasonal cycles between 10°N-40°N compared to the MLS and GEOSCCM. These indicate that
340 the 100-hPa seasonal oscillation between 10°N-40°N is too large to be simply explained by TTL temperatures.

341 Recent studies suggested that evaporation of convective ice in the TTL also contributes to the amount of water vapor
342 entering the stratosphere (Nielsen et al., 2007; Corti et al., 2008; Steinwagner et al., 2010; Dessler et al., 2016; Ueyama et
343 al., 2015, 2018 Schoeberl et al., 2014, 2018; Ye et al., 2018). To better understand this, we analyze a chemistry-climate
344 model where evaporation of convective ice is known to add water to the TTL (Dessler et al., 2016; Ye et al., 2018). Previous
345 work (Ye et al., 2018) has shown that the behavior of the GEOSCCM in the TTL is reasonable and agrees well with
346 observations. Comparisons with Cloud-Aerosol Lidar with Orthogonal Polarization (CALIOP) observations (Hu et al., 2009;
347 Liu et al., 2009; Vaughan et al., 2009; Winker et al., 2009, 2010; Young and Vaughan, 2009; Avery et al., 2012; Heymsfield
348 et al., 2014) show that the GEOSCCM IWC has too much ice in the TTL, but we used two sensitivity tests to show that our
349 results are not sensitive too these disagreements.

350 Using a version of the trajectory model driven by GEOSCCM meteorology that includes evaporation of GEOSCCM
351 convective ice, we obtained a more accurately simulated seasonal cycle of the 100-hPa water vapor between 10°N-40°N and
352 the hemispheric asymmetry compared to the GEOSCCM. We showed results where the GEOSCCM's IWC is reduced to
353 20% of the original value, and that did not affect our conclusions. In addition, our results are also not sensitive to
354 GEOSCCM putting convective ice too high in altitude (above 90 hPa). In these runs, adding convective ice to the trajectory
355 model increases the 100-hPa 10°N-40°N seasonal maximum by 1.65 ppmv (44%), and increases the seasonal amplitude by
356 1.03 ppmv (112%). We note that our estimate of convective moistening in the NH subtropical seasonal cycle in the
357 GEOSCCM is larger than the value produced by previous studies based on observations (e.g., Ueyama et al., 2018). This
358 could be due to overestimates of IWC by the GEOSCCM or because the instant dehydration scheme and instant ice
359 evaporation scheme we use lead to a greater convective impact on water vapor values overall. Therefore we regard our
360 results as providing insight for understanding the observations, but we caution against assuming that the numbers we
361 calculate for ice evaporation in the GEOSCCM are quantitatively accurate estimates of our atmosphere's values.

362 The majority of the convective moistening at 100-hPa and between 10°N-40°N is contributed by convective ice evaporation
363 in the 10°N-40°N latitudinal range during boreal summer. The maximum convective ice evaporation in this region is due to
364 available convective ice and relative humidity low enough to allow it to evaporate (Dessler and Sherwood, 2004). Ice
365 evaporation between 10°N-40°N contributes to 63% and 59% of the net convective moistening in the 100-hPa 10°N-40°N
366 water vapor seasonal maximum value and seasonal amplitude. Between 10°N-40°N, the Asian monsoon region plays the
367 most important role in convective moistening by ice evaporation. Convective ice evaporation in other regions, including the

368 deep tropics between 10°S-10°N, has a smaller influence in 100-hPa water vapor between 10°N-40°N. However, since the
369 GEOSCCM underestimates the observed convective ice over the North American monsoon above 120 hPa (not shown), it is
370 likely that this causes an underestimation of the moistening effect of convective ice over the North American region.
371 Previous studies showed that the ratio of isotopic water vapor (HDO), an indicator of sublimation of convective ice and in-
372 mixing (e.g., Dessler et al., 2007; Hanisco et al., 2007; Randel et al., 2012), enhances over the American monsoon region
373 during boreal summer, suggesting more convective ice evaporation there (Randel et al., 2012). This paper does not discuss
374 the HDO issue, and more work needs to be done in the future.

375 To summarize, we find that TTL temperature variations alone cannot explain the seasonal cycle of water vapor at 100 hPa in
376 MLS observations over the NH subtropics, 10°N-40°N (although temperature does explain the seasonal cycle in the tropics,
377 10°S-10°N and southern subtropics, 10°S-40°S). To try to understand the other mechanisms at work, we analyze a
378 chemistry-climate model, the GEOSCCM, which reproduces the MLS observations and has been shown to accurately
379 simulate the TTL. We find that, in the GEOSCCM, evaporation of convective ice in the TTL is responsible for the larger
380 seasonal cycle in the 100-hPa NH subtropics. We therefore conclude that evaporation of convective ice in the TTL, mainly
381 in boreal summer, is the most likely explanation for the observed larger seasonal cycle in the NH subtropics. We concur that
382 the seasonal cycle of the TTL temperatures is the major driver of the seasonal cycle of water vapor entering the stratosphere,
383 but we find that the contribution from evaporation of convective ice fills in more details of this simple picture. Our findings
384 emphasize the need to better understand and quantify the magnitude and spatial pattern of convective ice evaporation in the
385 TTL.

386 *Data availability.* The water vapor observed by MLS is available from <https://mls.jpl.nasa.gov/>. The ice water content
387 observed by CALIOP is available from <https://eosweb.larc.nasa.gov/>. The MERRA-2 meteorological fields are available
388 from <https://disc.gsfc.nasa.gov/>. The ERAi meteorological fields are available from
389 <https://www.ecmwf.int/en/forecasts/datasets/reanalysis-datasets/era-interim>.

390 *Competing interests.* The authors declare that they have no conflict of interest.

391 *Author contribution.* Xun Wang performed analysis, and wrote the original draft. Andrew E. Dessler provided the
392 conceptualization, guidance, and editing. Mark R. Schoeberl and Tao Wang contributed to the trajectory model code,
393 methodology, discussion, and editing. Wandu Yu contributed to methodology and discussion.

394 *Acknowledgments.* This work was supported by NASA grants NNX16AM15G and 80NSSC18K0134, both to Texas A&M
395 University. We would like to thank Dr. Luke Oman for providing the GEOSCCM meteorological fields used in this study.

396 **References**

397 Avery, M., Winker, D., Heymsfield, A., Vaughan, M., Young, S., Hu, Y. and Trepte, C.: Cloud ice water content retrieved
398 from the CALIOP space-based lidar, *Geophys. Res. Lett.*, 39(5), n/a-n/a, doi:10.1029/2011gl050545, 2012.

399 Avery, M. A., Davis, S. M., Rosenlof, K. H., Ye, H. and Dessler, A. E.: Large anomalies in lower stratospheric water vapour
400 and ice during the 2015–2016 El Niño, *Nat. Geosci.*, 10(6), 405–409, doi:10.1038/ngeo2961, 2017.

401 Bacmeister, J. T., Suarez, M. J. and Robertson, F. R.: Rain Reevaporation, Boundary Layer–Convection Interactions, and
402 Pacific Rainfall Patterns in an AGCM, *J. Atmos. Sci.*, 63(12), 3383–3403, doi:10.1175/JAS3791.1, 2006.

403 Bannister, R. N., O’Neill, A., Gregory, A. R. and Nissen, K. M.: The role of the south-east Asian monsoon and other
404 seasonal features in creating the ‘tape-recorder’ signal in the Unified Model, *Q. J. R. Meteorol. Soc.*, 130(599), 1531–
405 1554, doi:10.1256/qj.03.106, 2004.

406 Barahona, D., Molod, A., Bacmeister, J., Nenes, A., Gettelman, A., Morrison, H., Phillips, V. and Eichmann, A.:
407 Development of two-moment cloud microphysics for liquid and ice within the NASA Goddard Earth Observing System
408 Model (GEOS-5), *Geosci. Model Dev.*, 7(4), 1733–1766, doi:10.5194/gmd-7-1733-2014, 2014.

409 Bian, J., Pan, L. L., Paulik, L., Vömel, H., Chen, H. and Lu, D.: In situ water vapor and ozone measurements in Lhasa and
410 Kunming during the Asian summer monsoon, *Geophys. Res. Lett.*, 39(19), n/a–n/a, doi:10.1029/2012GL052996, 2012.

411 Bowman, K. P.: Large-scale isentropic mixing properties of the Antarctic polar vortex from analyzed winds, *J. Geophys.*
412 *Res. Atmos.*, 98(D12), 23013–23027, doi:10.1029/93JD02599, 1993.

413 Bowman, K. P. and Carrie, G. D.: The mean-meridional transport circulation of the troposphere in an idealized {GCM}, *J.*
414 *Atmos. Sci.*, 59(9), 1502–1514, doi:10.1175/1520-0469(2002)059<1502:TMMTCO>2.0.CO;2, 2002.

415 Brewer, A. W.: Evidence for a world circulation provided by the measurements of helium and water vapour distribution in
416 the stratosphere, *Q. J. R. Meteorol. Soc.*, 75(326), 351–363, doi:10.1002/qj.49707532603, 1949.

417 Corti, T., Luo, B. P., de Reus, M., Brunner, D., Cairo, F., Mahoney, M. J., Martucci, G., Matthey, R., Mitev, V., dos Santos,
418 F. H., Schiller, C., Shur, G., Sitnikov, N. M., Spelten, N., Vössing, H. J., Borrmann, S. and Peter, T.: Unprecedented
419 evidence for deep convection hydrating the tropical stratosphere, *Geophys. Res. Lett.*, 35(10), n/a–n/a,
420 doi:10.1029/2008GL033641, 2008.

421 Dessler, A. E. and Sherwood, S. C.: Effect of convection on the summertime extratropical lower stratosphere, *J. Geophys.*
422 *Res. Atmos.*, 109(D23), doi:10.1029/2004JD005209, 2004.

423 Dessler, A. E., Hanisco, T. F. and Fueglistaler, S.: Effects of convective ice lofting on H₂O and HDO in the tropical
424 tropopause layer, *J. Geophys. Res.*, 112(D18), D18309, doi:10.1029/2007JD008609, 2007.

425 Dessler, A. E., Ye, H., Wang, T., Schoeberl, M. R., Oman, L. D., Douglass, A. R., Butler, A. H., Rosenlof, K. H., Davis, S.
426 M. and Portmann, R. W.: Transport of ice into the stratosphere and the humidification of the stratosphere over the 21st
427 century, *Geophys. Res. Lett.*, 43(5), 2323–2329, doi:10.1002/2016GL067991, 2016.

428 Dethof, A., O’Neill, A., Slingo, J. M. and Smit, H. G. J.: A mechanism for moistening the lower stratosphere involving the
429 Asian summer monsoon, *Q. J. R. Meteorol. Soc.*, 125(556), 1079–1106, doi:10.1002/qj.1999.49712555602, 1999.

430 Dvortsov, V. L. and Solomon, S.: Response of the stratospheric temperatures and ozone to past and future increases in
431 stratospheric humidity, *J. Geophys. Res. Atmos.*, 106(D7), 7505–7514, doi:10.1029/2000JD900637, 2001.

432 Fu, R., Hu, Y., Wright, J. S., Jiang, J. H., Dickinson, R. E., Chen, M., Filipiak, M., Read, W. G., Waters, J. W. and Wu, D.
433 L.: Short circuit of water vapor and polluted air to the global stratosphere by convective transport over the Tibetan
434 Plateau, , 103(15), 5664–5669, doi:10.1073/pnas.0601584103, 2006.

435 Fueglistaler, S.: Stratospheric water vapor predicted from the Lagrangian temperature history of air entering the stratosphere
436 in the tropics, *J. Geophys. Res.*, 110(D8), D08107, doi:10.1029/2004JD005516, 2005.

437 Fueglistaler, S., Dessler, A. E., Dunkerton, T. J., Folkins, I., Fu, Q. and Mote, P. W.: Tropical tropopause layer, *Rev.*
438 *Geophys.*, 47, 1–31, doi:10.1029/2008RG000267, 2009.

439 Gelaro, R., McCarty, W., Suárez, M. J., Todling, R., Molod, A., Takacs, L., Randles, C. A., Darmenov, A., Bosilovich, M.
440 G., Reichle, R., Wargan, K., Coy, L., Cullather, R., Draper, C., Akella, S., Buchard, V., Conaty, A., da Silva, A. M., Gu,
441 W., Kim, G.-K., Koster, R., Lucchesi, R., Merkova, D., Nielsen, J. E., Partyka, G., Pawson, S., Putman, W., Rienecker,
442 M., Schubert, S. D., Sienkiewicz, M. and Zhao, B.: The Modern-Era Retrospective Analysis for Research and
443 Applications, Version 2 (MERRA-2), *J. Clim.*, 30(14), 5419–5454, doi:10.1175/JCLI-D-16-0758.1, 2017.

444 Gent, P. R., Danabasoglu, G., Donner, L. J., Holland, M. M., Hunke, E. C., Jayne, S. R., Lawrence, D. M., Neale, R. B.,
445 Rasch, P. J., Vertenstein, M., Worley, P. H., Yang, Z.-L. and Zhang, M.: The Community Climate System Model
446 Version 4, *J. Clim.*, 24(19), 4973–4991, doi:10.1175/2011JCLI4083.1, 2011.

447 Gettelman, A., Kinnison, D. E., Dunkerton, T. J. and Brasseur, G. P.: Impact of monsoon circulations on the upper
448 troposphere and lower stratosphere, *J. Geophys. Res. Atmos.*, 109(D22), doi:10.1029/2004JD004878, 2004.

449 Hanisco, T. F., Moyer, E. J., Weinstock, E. M., St. Clair, J. M., Sayres, D. S., Smith, J. B., Lockwood, R., Anderson, J. G.,
450 Dessler, A. E., Keutsch, F. N., Spackman, J. R., Read, W. G. and Bui, T. P.: Observations of deep convective influence
451 on stratospheric water vapor and its isotopic composition, *Geophys. Res. Lett.*, 34(4), L04814,
452 doi:10.1029/2006GL027899, 2007.

453 Heymsfield, A., Winker, D., Avery, M., Vaughan, M., Diskin, G., Deng, M., Mitev, V. and Matthey, R.: Relationships
454 between Ice Water Content and Volume Extinction Coefficient from In Situ Observations for Temperatures from 0° to
455 -86°C: Implications for Spaceborne Lidar Retrievals*, *J. Appl. Meteorol. Climatol.*, 53(2), 479–505,
456 doi:10.1175/JAMC-D-13-087.1, 2014.

457 Holton, J. R., Haynes, P. H., McIntyre, M. E., Douglass, A. R., Rood, R. B. and Pfister, L.: Stratosphere-troposphere
458 exchange, *Rev. Geophys.*, 33(4), 403, doi:10.1029/95RG02097, 1995.

459 Hu, Y., Winker, D., Vaughan, M., Lin, B., Omar, A., Trepte, C., Flittner, D., Yang, P., Nasiri, S. L., Baum, B., Holz, R.,
460 Sun, W., Liu, Z., Wang, Z., Young, S., Stammes, K., Huang, J. and Kuehn, R.: CALIPSO/CALIOP Cloud Phase
461 Discrimination Algorithm, *J. Atmos. Ocean. Technol.*, 26(11), 2293–2309, doi:10.1175/2009JTECHA1280.1, 2009.

462 Jackson, D. R., Driscoll, S. J., Highwood, E. J., Harries, J. E. and Russell, J. M.: Troposphere to stratosphere transport at low
463 latitudes as studies using HALOE observations of water vapour 1992–1997, *Q. J. R. Meteorol. Soc.*, 124(545), 169–192,
464 doi:10.1002/qj.49712454508, 1998.

465 James, R., Bonazzola, M., Legras, B., Surbled, K. and Fueglistaler, S.: Water vapor transport and dehydration above
466 convective outflow during Asian monsoon, *Geophys. Res. Lett.*, 35(20), doi:10.1029/2008GL035441, 2008.

467 Jensen, E. J., Diskin, G., Lawson, R. P., Lance, S., Bui, T. P., Hlavka, D., McGill, M., Pfister, L., Toon, O. B. and Gao, R.:
468 Ice nucleation and dehydration in the Tropical Tropopause Layer, *Proc. Natl. Acad. Sci.*, 110(6), 2041–2046,
469 doi:10.1073/pnas.1217104110, 2013.

470 Kärcher, B., Hendricks, J. and Lohmann, U.: Physically based parameterization of cirrus cloud formation for use in global
471 atmospheric models, *J. Geophys. Res.*, 111(D1), D01205, doi:10.1029/2005JD006219, 2006.

472 Lambert, A., Read, W. G., Livesey, N. J., Santee, M. L., Manney, G. L., Froidevaux, L., Wu, D. L., Schwartz, M. J.,
473 Pumphrey, H. C., Jimenez, C., Nedoluha, G. E., Cofield, R. E., Cuddy, D. T., Daffer, W. H., Drouin, B. J., Fuller, R. A.,
474 Jarnot, R. F., Knosp, B. W., Pickett, H. M., Perun, V. S., Snyder, W. V., Stek, P. C., Thurstans, R. P., Wagner, P. A.,
475 Waters, J. W., Jucks, K. W., Toon, G. C., Stachnik, R. A., Bernath, P. F., Boone, C. D., Walker, K. A., Urban, J.,
476 Murtagh, D., Elkins, J. W. and Atlas, E.: Validation of the Aura Microwave Limb Sounder middle atmosphere water
477 vapor and nitrous oxide measurements, *J. Geophys. Res. Atmos.*, 112(D24), D24S36, doi:10.1029/2007JD008724,
478 2007.

479 Liu, Z., Vaughan, M., Winker, D., Kittaka, C., Getzewich, B., Kuehn, R., Omar, A., Powell, K., Trepte, C. and Hostetler, C.:
480 The CALIPSO Lidar Cloud and Aerosol Discrimination: Version 2 Algorithm and Initial Assessment of Performance, *J.*
481 *Atmos. Ocean. Technol.*, 26(7), 1198–1213, doi:10.1175/2009JTECHA1229.1, 2009.

482 Livesey, N. J., Read, W. G., Wagner, P. A., Froidevaux, L., Lambert, A., Manney, G. L., Millán-Valle, L. F., Pumphrey, H.
483 C., Santee, M. L., Schwartz, M. J., Wang, S., Fuller, R. A., Jarnot, R. F., Knosp, B. W., and Martinez, E.: Earth
484 Observing System (EOS) Aura Microwave Limb Sounder (MLS), Version 4.2x Level 2 data quality and description
485 document, Tech. Rep. JPL D-33509, Tech. Rep. version 4.2x-3.0, NASA Jet Propulsion Laboratory, 2017.

486 Luo, J., Pan, L. L., Honomichl, S. B., Bergman, J. W., Randel, W. J., Francis, G., Clerbaux, C., George, M., Liu, X. and
487 Tian, W.: Space-time variability in UTLS chemical distribution in the Asian summer monsoon viewed by limb and
488 nadir satellite sensors, *Atmos. Chem. Phys.*, 18(16), 12511–12530, doi:10.5194/acp-18-12511-2018, 2018.

489 Molod, A., Takacs, L., Suarez, M., Bacmeister, J., Song, I.-S., and Eichmann, A.: The GEOS-5 atmospheric general
490 circulation model: Mean climate and development from MERRA to Fortuna, Technical Report Series on Global
491 Modeling and Data Assimilation Volume 28, NASA Goddard Space Flight Center, 2012.

492 Molod, A., Takacs, L., Suarez, M. and Bacmeister, J.: Development of the GEOS-5 atmospheric general circulation model:
493 evolution from MERRA to MERRA2, *Geosci. Model Dev.*, 8(5), 1339–1356, doi:10.5194/gmd-8-1339-2015, 2015.

494 Mote, P. W., Rosenloh, K. H., Holton, J. R., Harwood, R. S. and Waters, J. W.: Seasonal variations of water vapor in the
495 tropical lower stratosphere, *Geophys. Res. Lett.*, 22(9), 1093–1096, doi:10.1029/95GL01234, 1995.

496 Mote, P. W., Rosenlof, K. H., McIntyre, M. E., Carr, E. S., Gille, J. C., Holton, J. R., Kinnery, J. S., Pumphrey, H. C.,
497 Russell III, J. M. and Waters, J. W.: An atmospheric tape recorder: The imprint of tropical tropopause temperatures on
498 stratospheric water vapor, *J. Geophys. Res.*, 101(D2), 3989–4006, doi:10.1029/95JD03422, 1996.

499 Moyer, E. J., Irion, F. W., Yung, Y. L. and Gunson, M. R.: ATMOS stratospheric deuterated water and implications for
500 troposphere-stratosphere transport, *Geophys. Res. Lett.*, 23(17), 2385–2388, doi:10.1029/96GL01489, 1996.

501 Murphy, D. M. and Koop, T.: Review of the vapour pressures of ice and supercooled water for atmospheric applications, *Q.*
502 *J. R. Meteorol. Soc.*, 131(608), 1539–1565, doi:10.1256/qj.04.94, 2005.

503 Nielsen, J. K., Larsen, N., Cairo, F., Donfrancesco, G. Di, Rosen, J. M., Durrý, G., Held, G. and Pommereau, J.-P.: Solid
504 particles in the tropical lowest stratosphere, *Atmos. Chem. Phys.*, 7(3), 685–695, doi:10.5194/acp-7-685-2007, 2007.

505 Oman, L. D. and Douglass, A. R.: Improvements in total column ozone in GEOSCCM and comparisons with a new ozone-
506 depleting substances scenario, *J. Geophys. Res. Atmos.*, 119(9), 5613–5624, doi:10.1002/2014JD021590, 2014.

507 Pan, L., Solomon, S., Randel, W., Lamarque, J.-F., Hess, P., Gille, J., Chiou, E.-W. and McCormick, M. P.: Hemispheric
508 asymmetries and seasonal variations of the lowermost stratospheric water vapor and ozone derived from SAGE II data,
509 *J. Geophys. Res. Atmos.*, 102(D23), 28177–28184, doi:10.1029/97JD02778, 1997.

510 Pan, L. L., Hintsä, E. J., Stone, E. M., Weinstock, E. M. and Randel, W. J.: The seasonal cycle of water vapor and saturation
511 vapor mixing ratio in the extratropical lowermost stratosphere, *J. Geophys. Res. Atmos.*, 105(D21), 26519–26530,
512 doi:10.1029/2000JD900401, 2000.

513 Pan, L. L., Honomichl, S. B., Kinnison, D. E., Abalos, M., Randel, W. J., Bergman, J. W. and Bian, J.: Transport of chemical
514 tracers from the boundary layer to stratosphere associated with the dynamics of the Asian summer monsoon, *J.*
515 *Geophys. Res. Atmos.*, 121(23), 14,159–14,174, doi:10.1002/2016JD025616, 2016.

516 Park, M., Randel, W. J., Kinnison, D. E., Garcia, R. R. and Choi, W.: Seasonal variation of methane, water vapor, and
517 nitrogen oxides near the tropopause: Satellite observations and model simulations, *J. Geophys. Res. Atmos.*, 109(D3),
518 n/a-n/a, doi:10.1029/2003JD003706, 2004.

519 Park, M., Randel, W. J., Gettelman, A., Massie, S. T. and Jiang, J. H.: Transport above the Asian summer monsoon
520 anticyclone inferred from Aura Microwave Limb Sounder tracers, *J. Geophys. Res. Atmos.*, 112(D16), 2007.

521 Pawson, S., Stolarski, R. S., Douglass, A. R., Newman, P. A., Nielsen, J. E., Frith, S. M. and Gupta, M. L.: Goddard Earth
522 Observing System chemistry-climate model simulations of stratospheric ozone-temperature coupling between 1950 and
523 2005, *J. Geophys. Res.*, 113(D12), D12103, doi:10.1029/2007JD009511, 2008.

524 Ploeger, F., Günther, G., Konopka, P., Fueglistaler, S., Müller, R., Hoppe, C., Kunz, A., Spang, R., Groöß, J.-U. and Riese,
525 M.: Horizontal water vapor transport in the lower stratosphere from subtropics to high latitudes during boreal summer, *J.*
526 *Geophys. Res. Atmos.*, 118(14), 8111–8127, doi:10.1002/jgrd.50636, 2013.

527 Randel, W. J. and Park, M.: Deep convective influence on the Asian summer monsoon anticyclone and associated tracer
528 variability observed with Atmospheric Infrared Sounder (AIRS), *J. Geophys. Res.*, 111(D12), D12314,
529 doi:10.1029/2005JD006490, 2006.

530 Randel, W. J., Wu, F., Russell, J. M., Roche, A. and Waters, J. W.: Seasonal Cycles and QBO Variations in Stratospheric
531 CH₄ and H₂O Observed in UARS HALOE Data, *J. Atmos. Sci.*, 55(2), 163–185, doi:10.1175/1520-
532 0469(1998)055<0163:Scaqvi>2.0.Co;2, 1998.

533 Randel, W. J., Wu, F., Gettelman, A., Russell, J. M., Zawodny, J. M. and Oltmans, S. J.: Seasonal variation of water vapor in
534 the lower stratosphere observed in Halogen Occultation Experiment data, *J. Geophys. Res. Atmos.*, 106(D13), 14313–
535 14325, doi:10.1029/2001jd900048, 2001.

536 Randel, W. J., Moyer, E., Park, M., Jensen, E., Bernath, P., Walker, K. and Boone, C.: Global variations of HDO and
537 HDO/H₂O ratios in the upper troposphere and lower stratosphere derived from ACE-FTS satellite measurements, *J.*
538 *Geophys. Res. Atmos.*, 117(D6), n/a-n/a, doi:10.1029/2011JD016632, 2012.

539 Randel, W. J., Zhang, K. and Fu, R.: What controls stratospheric water vapor in the NH summer monsoon regions?, *J.*
540 *Geophys. Res. Atmos.*, 120(15), 7988–8001, doi:10.1002/2015JD023622, 2015.

541 Rienecker, M.M., Suarez, M.J., Todling, R., Bacmeister, J., Takacs, L., Liu, H.-C., Gu, W., Sienkiewicz, M., Koster, R.D.,
542 Gelaro, R., Stajner, I., and Nielsen J.E.: The GEOS-5 data assimilation system—Documentation of versions 5.0.1, 5.1.0,
543 and 5.2.0, Technical Report Series on Global Modeling and Data Assimilation, Volume 27, NASA Goddard Space
544 Flight Center Greenbelt, 2008.

545 Rosenlof, K. H.: Hemispheric asymmetries in water vapor and inferences about transport in the lower stratosphere, *J.*
546 *Geophys. Res. Atmos.*, 102(D11), 13213–13234, doi:10.1029/97JD00873, 1997.

547 Schoeberl, M., Dessler, A., Ye, H., Wang, T., Avery, M. and Jensen, E.: The impact of gravity waves and cloud nucleation
548 threshold on stratospheric water and tropical tropospheric cloud fraction, *Earth Sp. Sci.*, 3(8), 295–305,

549 doi:10.1002/2016EA000180, 2016.

550 Schoeberl, M. R. and Dessler, A. E.: Dehydration of the stratosphere, *Atmos. Chem. Phys.*, 11(16), 8433–8446,
551 doi:10.5194/acp-11-8433-2011, 2011.

552 Schoeberl, M. R., Douglass, A. R., Newman, P. A., Lait, L. R., Lary, D., Waters, J., Livesey, N., Froidevaux, L., Lambert,
553 A., Read, W., Filipiak, M. J. and Pumphrey, H. C.: QBO and annual cycle variations in tropical lower stratosphere trace
554 gases from HALOE and Aura MLS observations, *J. Geophys. Res. Atmos.*, 113(D5), n/a-n/a,
555 doi:10.1029/2007JD008678, 2008.

556 Schoeberl, M. R., Dessler, A. E. and Wang, T.: Modeling upper tropospheric and lower stratospheric water vapor anomalies,
557 *Atmos. Chem. Phys.*, 13(15), 7783–7793, doi:10.5194/acp-13-7783-2013, 2013.

558 Schoeberl, M. R., Dessler, A. E., Wang, T., Avery, M. A. and Jensen, E. J.: Cloud formation, convection, and stratospheric
559 dehydration, *Earth Sp. Sci.*, 1(1), 1–17, doi:10.1002/2014EA000014, 2014.

560 Schoeberl, M. R., Jensen, E. J. and Woods, S.: Gravity waves amplify upper tropospheric dehydration by clouds, *Earth Sp.*
561 *Sci.*, 2(12), 485–500, doi:10.1002/2015EA000127, 2015.

562 Schoeberl, M. R., Jensen, E. J., Pfister, L., Ueyama, R., Avery, M. and Dessler, A. E.: Convective Hydration of the Upper
563 Troposphere and Lower Stratosphere, *J. Geophys. Res. Atmos.*, 123(9), 4583–4593, doi:10.1029/2018JD028286, 2018.

564 Schoeberl, M. R., Jensen, E. J., Pfister, L., Ueyama, R., Wang, T., Selkirk, H., Avery, M., Thornberry, T. and Dessler, A. E.:
565 Water Vapor, Clouds, and Saturation in the Tropical Tropopause Layer, *J. Geophys. Res. Atmos.*, 124(7), 3984–4003,
566 doi:10.1029/2018JD029849, 2019.

567 Schwartz, M. J., Read, W. G., Santee, M. L., Livesey, N. J., Froidevaux, L., Lambert, A. and Manney, G. L.: Convectively
568 injected water vapor in the North American summer lowermost stratosphere, *Geophys. Res. Lett.*, 40(10), 2316–2321,
569 doi:10.1002/grl.50421, 2013.

570 Solomon, S., Garcia, R. R., Rowland, F. S. and Wuebbles, D. J.: On the depletion of Antarctic ozone, *Nature*, 321(6072),
571 755–758, doi:10.1038/321755a0, 1986.

572 Steinwagner, J., Fueglistaler, S., Stiller, G., von Clarmann, T., Kiefer, M., Borsboom, P.-P., van Delden, A. and Röckmann,
573 T.: Tropical dehydration processes constrained by the seasonality of stratospheric deuterated water, *Nat. Geosci.*, 3, 262,
574 doi:10.1038/ngeo822, 2010.

575 Ueyama, R., Jensen, E. J., Pfister, L. and Kim, J.-E.: Dynamical, convective, and microphysical control on wintertime
576 distributions of water vapor and clouds in the tropical tropopause layer, *J. Geophys. Res. Atmos.*, 120(19), 10,410-
577 483,500, doi:10.1002/2015JD023318, 2015.

578 Ueyama, R., Jensen, E. J. and Pfister, L.: Convective Influence on the Humidity and Clouds in the Tropical Tropopause
579 Layer During Boreal Summer, *J. Geophys. Res. Atmos.*, doi:10.1029/2018JD028674, 2018.

580 Vaughan, M. A., Powell, K. A., Winker, D. M., Hostetler, C. A., Kuehn, R. E., Hunt, W. H., Getzewich, B. J., Young, S. A.,
581 Liu, Z. and McGill, M. J.: Fully Automated Detection of Cloud and Aerosol Layers in the CALIPSO Lidar
582 Measurements, *J. Atmos. Ocean. Technol.*, 26(10), 2034–2050, doi:10.1175/2009JTECHA1228.1, 2009.

583 Van Vuuren, D. P., Edmonds, J., Kainuma, M., Riahi, K., Thomson, A., Hibbard, K., Hurtt, G. C., Kram, T., Krey, V.,
584 Lamarque, J.-F. and others: The representative concentration pathways: an overview, *Clim. Change*, 109, 5–31,
585 doi:10.1007/s10584-011-0148-z, 2011.

586 Winker, D. M., Vaughan, M. A., Omar, A., Hu, Y., Powell, K. A., Liu, Z., Hunt, W. H. and Young, S. A.: Overview of the
587 CALIPSO Mission and CALIOP Data Processing Algorithms, *J. Atmos. Ocean. Technol.*, 26(11), 2310–2323,
588 doi:10.1175/2009jtechna1281.1, 2009.

589 Winker, D. M., Pelon, J., Coakley, J. A., Ackerman, S. A., Charlson, R. J., Colarco, P. R., Flamant, P., Fu, Q., Hoff, R. M.,
590 Kittaka, C., Kubar, T. L., Le Treut, H., McCormick, M. P., Mégie, G., Poole, L., Powell, K., Trepte, C., Vaughan, M. A.
591 and Wielicki, B. A.: The CALIPSO Mission, *Bull. Am. Meteorol. Soc.*, 91(9), 1211–1230,
592 doi:10.1175/2010BAMS3009.1, 2010.

593 Woods, S., Lawson, R. P., Jensen, E., Bui, T. P., Thornberry, T., Rollins, A., Pfister, L. and Avery, M.: Microphysical
594 Properties of Tropical Tropopause Layer Cirrus, *J. Geophys. Res. Atmos.*, 123(11), 6053–6069,
595 doi:10.1029/2017JD028068, 2018.

596 World Meteorological Organization: Scientific assessment of ozone depletion, Global Ozone Research and Monitoring
597 Project–Report No. 52, Geneva, Switzerland, 2010.

598 Wright, J. S., Fu, R., Fueglistaler, S., Liu, Y. S. and Zhang, Y.: The influence of summertime convection over Southeast

599 Asia on water vapor in the tropical stratosphere, *J. Geophys. Res. Atmos.*, 116(D12), 1–12, doi:10.1029/2010JD015416,
600 2011.

601 Ye, H., Dessler, A. E. and Yu, W.: Effects of convective ice evaporation on interannual variability of tropical tropopause
602 layer water vapor, *Atmos. Chem. Phys.*, 18(7), 4425–4437, doi:10.5194/acp-18-4425-2018, 2018.

603 Young, S. A. and Vaughan, M. A.: The Retrieval of Profiles of Particulate Extinction from Cloud-Aerosol Lidar Infrared
604 Pathfinder Satellite Observations (CALIPSO) Data: Algorithm Description, *J. Atmos. Ocean. Technol.*, 26(6), 1105–
605 1119, doi:10.1175/2008JTECHA1221.1, 2009.

606

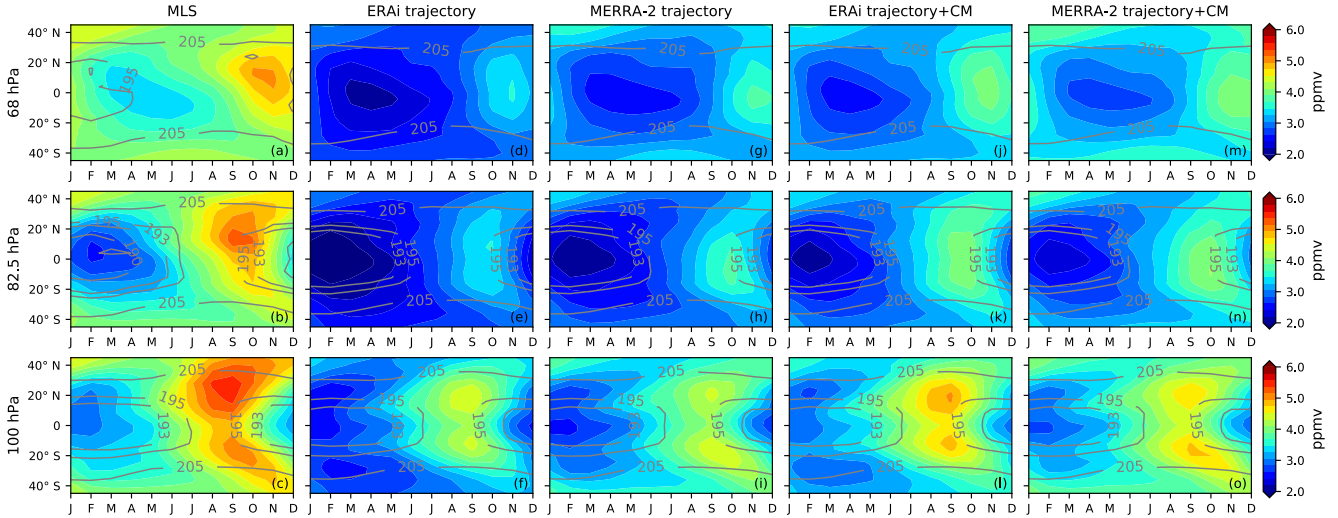
607 **Table 1: Summary of trajectory model cases**

Trajectory Model Cases	Description
ERAi standard trajectory model	Instant dehydration with no convective influence
MERRA-2 standard trajectory model	Instant dehydration with no convective influence
ERAi trajectory with cloud model	Dehydration with the cloud model, but with no convective influence
MERRA-2 trajectory with cloud model	Dehydration with the cloud model, but with no convective influence
GEOSCCM standard trajectory model	Instant dehydration with no convective influence
GEOSCCM ice model	Instant dehydration. Convective ice instantly evaporates to sub-saturated parcels
GEOSCCM 0.2ice model	Instant dehydration. GEOSCCM convective ice input is decreased by 80%. Convective ice instantly evaporates to sub-saturated parcels
GEOSCCM ice model below 90 hPa	Instant dehydration. Convective ice evaporation above the 90-hPa surface is not allowed

608

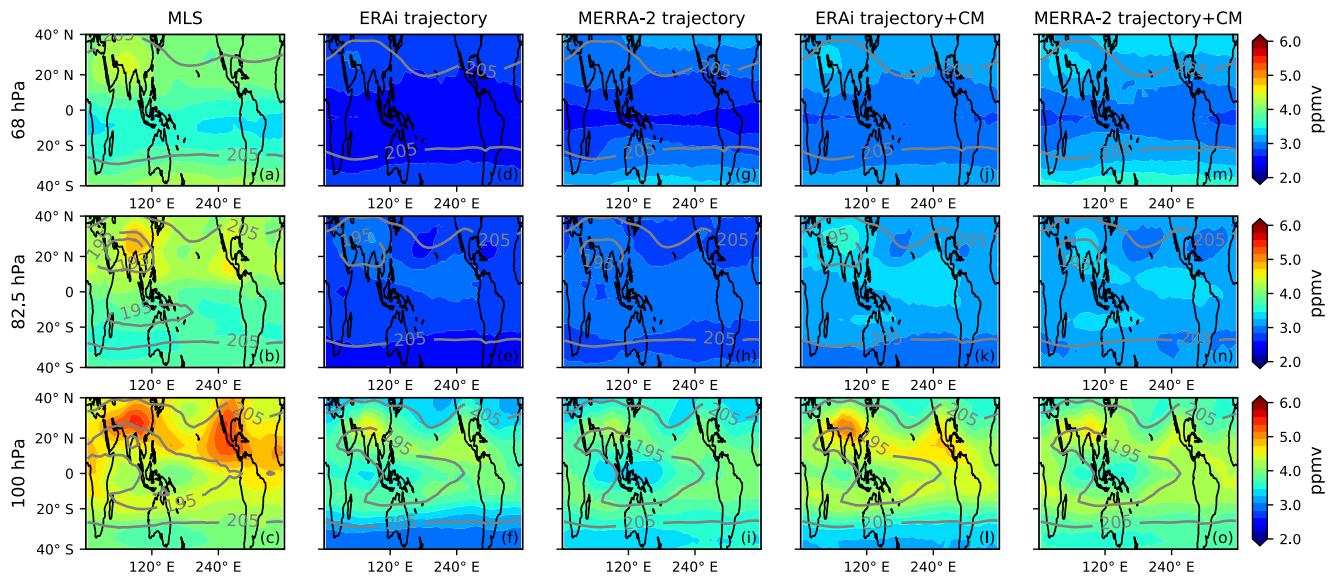
609

610



611

612 **Figure 1: Zonal mean seasonal cycle water vapor (ppmv, color shading) and temperature (K, contour lines) between 40°S - 40°N**
 613 **from (a)-(c) MLS, (d)-(f) ERAi trajectory model, (g)-(i) MERRA-2 trajectory model, (j)-(l) ERAi trajectory model with the**
 614 **cloud model, and (m)-(o) MERRA-2 trajectory model with the cloud model at 68 hPa (top row), 82.5 hPa (middle row) and 100 hPa**
 615 **(bottom row).**



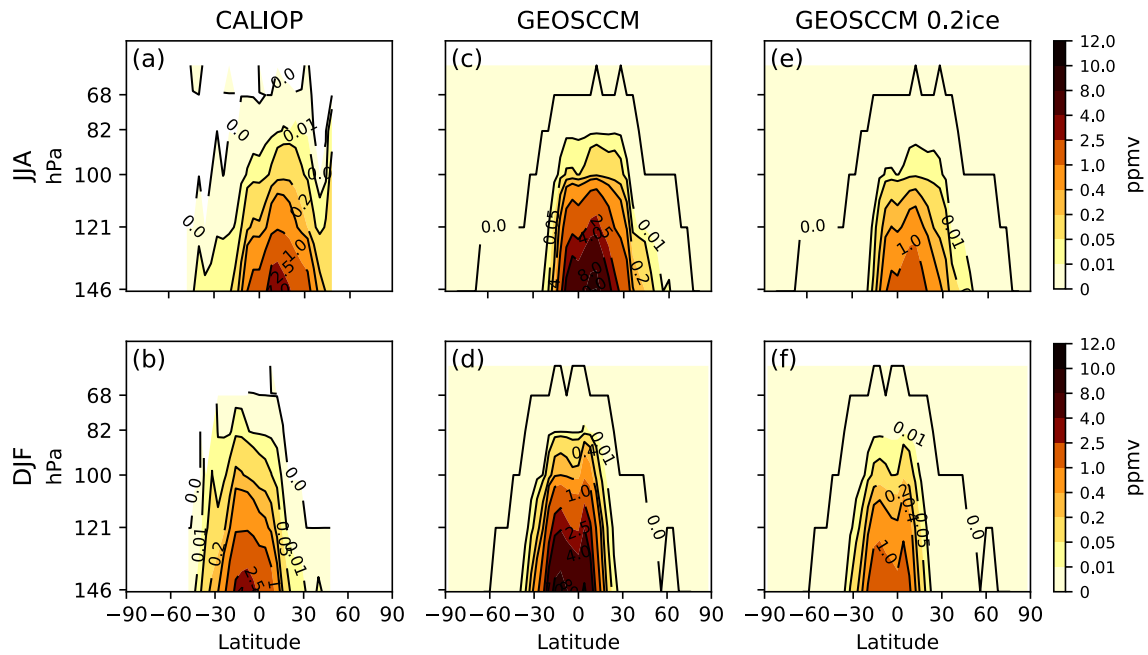
616
 617 **Figure 2: JJA water vapor (ppmv, color shading) and temperature (K, contour lines) between 40°S - 40°N from (a)-(c) MLS, (d)-(f)**
 618 **ERAi trajectory model, (g)-(i) MERRA-2 trajectory model, (j)-(l) ERAi trajectory model with the cloud model, and (m)-(o)**
 619 **MERRA-2 trajectory model with the cloud model at 68 hPa (top row), 82.5 hPa (middle row) and 100 hPa (bottom row).**

620

621

622

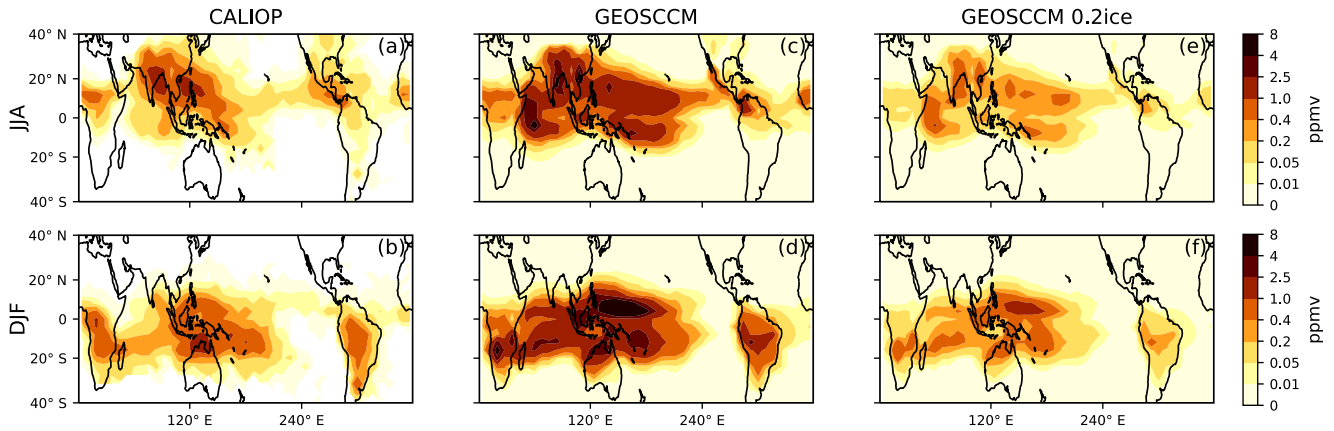
623



624

625 **Figure 3. Zonal mean convective IWC (ppmv) from CALIOP and GEOSCCM above 146 hPa. The CALIOP ice data is averaged**
 626 **over JJA (top row) and DJF (bottom row) from 200805 – 201312. For CALIOP ice data (a and b), we show the ice from all clouds**
 627 **minus the ice from cirrus clouds, which is a rough estimate of convective ice in the TTL region. For GEOSCCM ice, we show**
 628 **convective ice (c and d). To better match the tropical average CALIOP ice field above 120 hPa, we decrease the GEOSCCM ice by**
 629 **80% (0.2ice) and show them in panels e and f. Note we use a nonlinear color scale.**

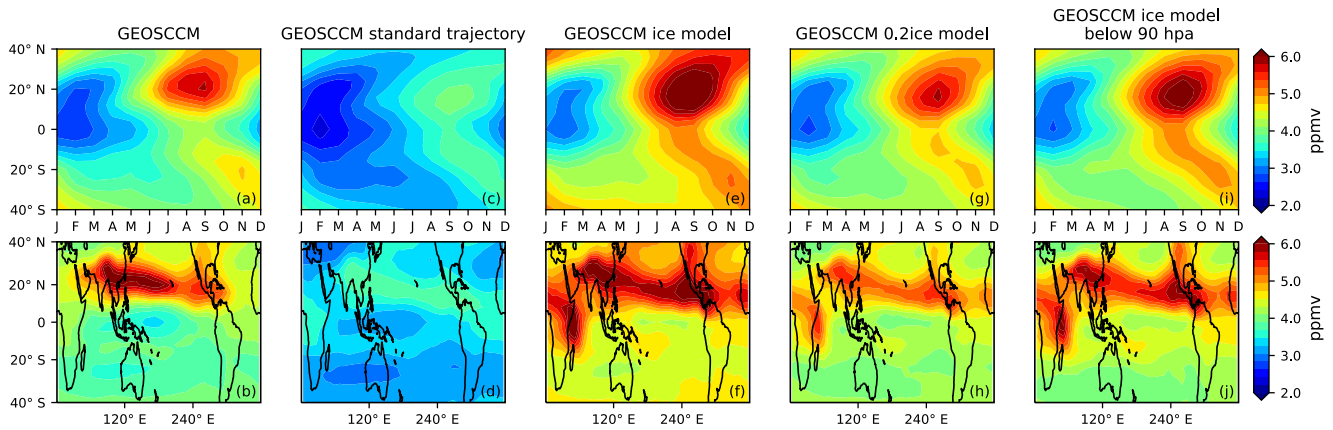
630



631

632 **Figure 4. Same as Fig. 3, but for convective IWC (ppmv) averaged between 121-82.5 hPa During JJA and DJF.**

633



635

636

637

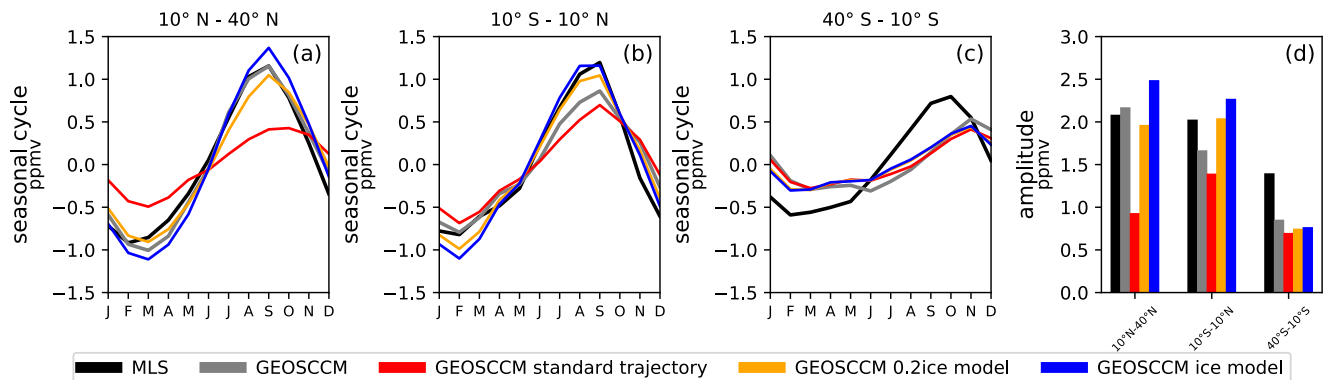
638

639

Figure 5. Top panel: Zonal mean seasonal cycle of 100-hPa water vapor (ppmv) between 40°S - 40°N from (a) GEOSCCM, (c) GEOSCCM standard model, (e) GEOSCCM ice model (g) GEOSCCM 0.2ice model, and (i) GEOSCCM ice model with ice below 90 hPa. Bottom panel: JJA 100-hPa water vapor (ppmv) between 40°S - 40°N from (b) GEOSCCM, (d) GEOSCCM standard model, (f) GEOSCCM ice model (h) GEOSCCM 0.2ice model, and (j) GEOSCCM ice model with ice below 90 hPa.

640

641



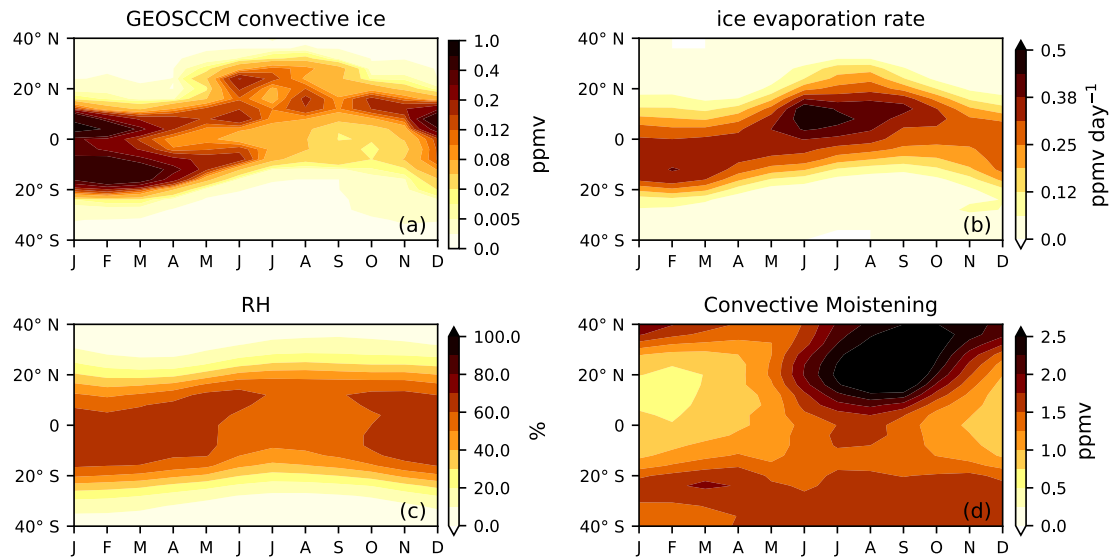
642

643

644

645

Figure 6. Seasonal cycles of water vapor at 100 hPa averaged between (a) 10°N-40°N, (b) 10°S-10°N, and (c) 40°S-10°S and their (d) seasonal amplitudes from GEOSCCM, GEOSCCM standard model, GEOSCCM ice model, and GEOSCCM 0.2ice model. We have subtracted the annual mean from each data set.



647

648

649

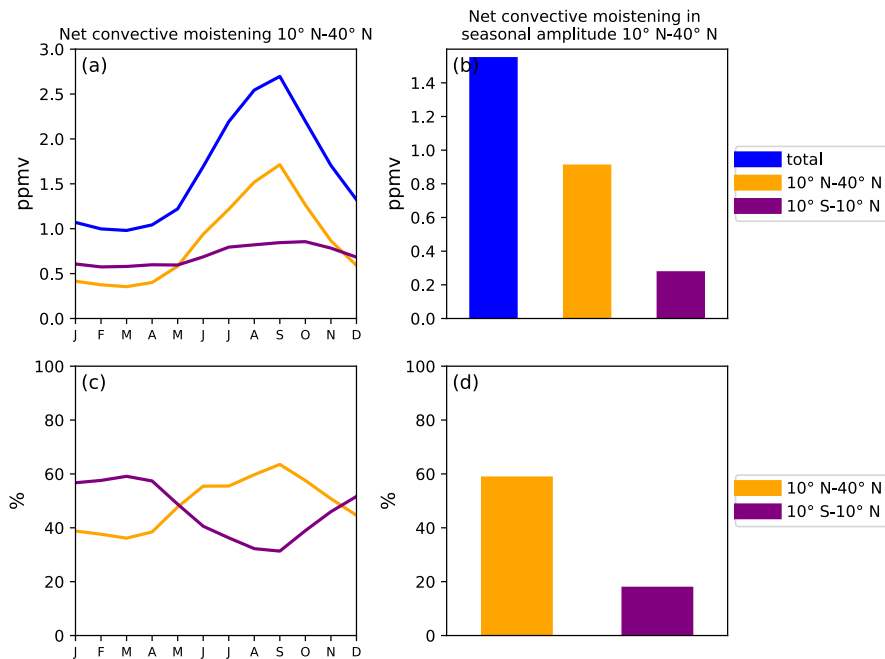
650

651

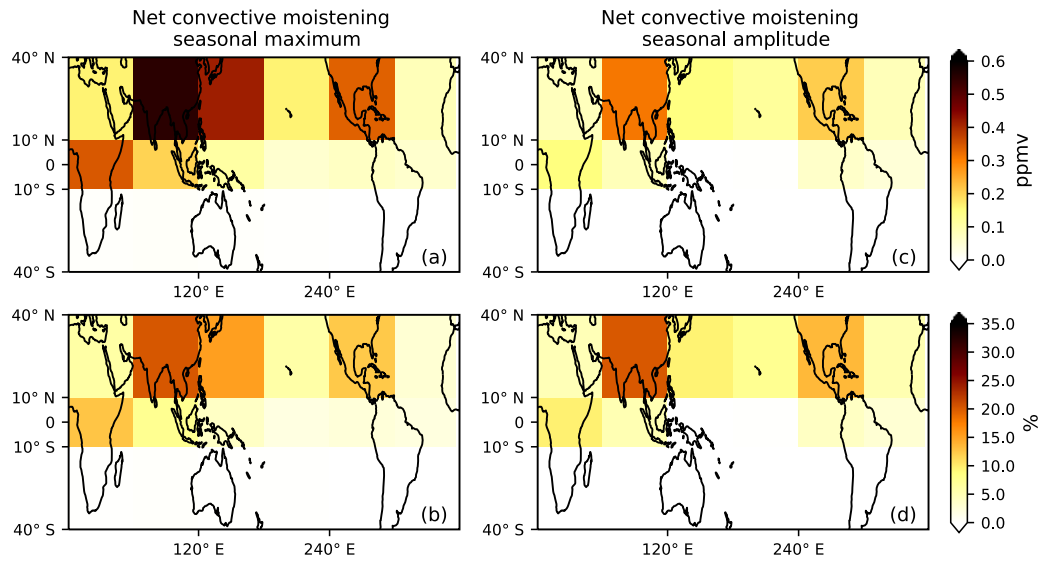
652

653

Figure 7. (a) Zonal mean seasonal cycle of 100-hPa convective ice (ppmv) from GEOSCCM. Note the color scale is nonlinear. (b) Zonal mean seasonal cycle of 100-hPa evaporation rate (ppmv day⁻¹) from the GEOSCCM ice model. (c) Zonal mean seasonal cycle of relative humidity (%) with respect to ice at 100 hPa from GEOSCCM. (d) Zonal mean seasonal cycle of net convective moistening (ppmv) at 100 hPa from the ice model. The quantity net convective moistening is the difference between water vapor values from the ice model and standard model.



655
 656 **Figure 8. (a) Net convective moistening (ppmv) in the 100-hPa 10°N-40°N water vapor seasonal cycle and the portions (ppmv)**
 657 **contributed by convective ice evaporation over 10°S-10°N and 10°N-40°N. (b) Net convective moistening (ppmv) in the 100-hPa**
 658 **10°N-40°N water vapor seasonal amplitude and the portions (ppmv) contributed by convective ice evaporation over 10°S-10°N and**
 659 **10°N-40°N. (c)-(d) Percentage of net convective moistening in the 100-hPa 10°N-40°N water vapor seasonal cycle and seasonal**
 660 **amplitude contributed by convective ice evaporation over 10°S-10°N and 10°N-40°N. The percentage is net convective moistening**
 661 **contributed by 10°S-10°N or 10°N-40°N region divided by the total net convective moistening.**



662
 663 **Figure 9. Portions of net convective moistening (ppmv) in the (a) maximum value and (b) seasonal amplitude of the 100-hPa 10°N-**
 664 **40°N water vapor seasonal cycle contributed by 12 equal-area box regions between 10°S-40°N. (c) and (d): Same as (a) and (b), but**
 665 **for the percentage of net convective moistening contributed by the 12 equal-area box regions.**